

Journal of Biomedical Optics

SPIEDigitalLibrary.org/jbo

Spatiotemporal analysis for indocyanine green-aided imaging of rheumatoid arthritis in hand joints

Pouyan Mohajerani
Reinhard Meier
Peter B. Noël
Ernst J. Rummeny
Vasilis Ntziachristos

Spatiotemporal analysis for indocyanine green-aided imaging of rheumatoid arthritis in hand joints

Pouyan Mohajerani,^a Reinhard Meier,^b Peter B. Noël,^b Ernst J. Rummeny,^b and Vasilis Ntziachristos^a

^aTechnische Universität München and Helmholtz Zentrum München, Institute for Biological and Medical Imaging, Ingolstädter Landstrasse 1, Neuherberg 85764, Germany

^bTechnische Universität München, Department of Radiology, Klinikum Rechts der Isar, Munich 81675, Germany

Abstract. Rheumatoid arthritis (RA) is the most common chronic inflammatory joint disease, with a prevalence of 0.5 to 1% in the general population. Imaging can possibly aid in early diagnosis, crucial to effective personalized therapeutic strategies and treatment follow-up. The intravenous administration of indocyanine green (ICG) has been considered for identifying synovial hyperperfusion as an RA physiological biomarker. However, while the distribution of ICG in the human hand is a time-dependent process, the particular biodistribution dynamic patterns established following intravenous administration have not yet been studied. For this reason, the dynamic relationships of ICG distribution in the human hand in RA patients using a method based on principal component analysis are analyzed. *In vivo* analyses were corroborated by simulations of clinical scenarios using a finite element method. Observations of spatiotemporal characteristics are contrasted to fluorescence intensity images and magnetic resonance images of the hand joints, employed as the anatomical and diagnostic reference. Processing results for 450 joints from 5 healthy volunteers and 10 patients show that image features obtained from the spatiotemporal analysis offer good congruence with synovitis and reveal better detection performance compared to observations of raw fluorescence intensity images. © 2013 Society of Photo-Optical Instrumentation Engineers (SPIE) [DOI: 10.1117/1.JBO.18.9.097004]

Keywords: rheumatoid arthritis; indocyanine green; planar fluorescence imaging; epi-illumination imaging; magnetic resonance imaging; finite element modeling; principal component analysis.

Paper 130188RR received Mar. 29, 2013; revised manuscript received Aug. 14, 2013; accepted for publication Aug. 19, 2013; published online Sep. 17, 2013.

1 Introduction

Rheumatoid arthritis (RA), the most common chronic form of arthritis,¹ is an autoimmune disease that affects up to 1% of the population. RA typically affects the synovial joint linings, triggering buildup of synovitis in joints, resulting in cartilage and bone damage. Imaging can play a significant role in the early diagnosis of RA and monitoring the effectiveness of a corresponding treatment.^{2,3} Conventionally, x-ray imaging has been employed for imaging RA features, such as bone and joint destruction as a result of inflammation. However, this approach is limited to imaging effects due to relatively advanced inflammation with visible bone damage.⁴ Magnetic resonance imaging (MRI) and ultrasound imaging are also employed as alternatives to x-ray imaging for early RA imaging. Promising results have been shown to make early diagnosis possible. Limitations include the high cost and long examination time (for MRI) or the operator dependency (for ultrasound).⁵

Optical imaging has been considered as an alternative RA imaging method, since it offers fast noninvasive imaging.⁶⁻¹⁴ Transillumination planar imaging using a 675-nm laser was considered to assess the progress of disease by observing human proximal interphalangeal (PIP) finger joints and evaluating features of the optical images collected using image classification algorithms.⁸ This approach was able to resolve inflammation in PIP joints in a group of 72 joints with 80% sensitivity and 89% specificity, and was shown to be better in assessing

inflammatory variations in the synovium. Optical tomography approaches have also been considered to three-dimensionally resolve optical coefficients changes between rheumatoid synovial tissue in rheumatoid PIP joints in comparison to healthy PIP joints.^{7,11,13,15,16} These methods aim at reconstructing the optical absorption and scattering coefficients in two-dimensional planes or three-dimensionally in finger joints and rely on the increase in the optical absorption and scattering due to clouding of the synovial fluid or membrane inflammation^{8,11} or measurement of water concentration and tissue oxygen saturation levels¹⁷ differentiate between arthritic and healthy joints. It was reported in Ref. 11 that the optical absorption and scattering of synovial tissue can increase up to an order of magnitude with inflammation, and frequency-domain diffuse optical tomography was shown to differentiate between healthy and arthritic joints with >85% sensitivity and specificity in a group of 99 PIP joints with rheumatoid arthritis and 120 healthy PIP joints.¹⁵ Diagnosis of osteoarthritis in distal interphalangeal (DIP) joints of 22 patients and 18 volunteers with 91% sensitivity and 100% specificity was demonstrated in Ref. 17 using an x-ray-guided multispectral technique. It should be noted that optoacoustic methods have also been proposed for imaging inflammatory arthritis and osteoarthritis in small animal and human joints.^{18,19} The aforementioned optical and optoacoustic planar or tomographic optical imaging methods have been limited to interphalangeal human finger joints. Laser Doppler imaging has further been proposed for imaging perfusion maps of microvasculature in PIP and metacarpophalangeal (MCP) human hand joints.^{20,21}

Address all correspondence to: Vasilis Ntziachristos, Technische Universität München and Helmholtz Zentrum München, Institute for Biological and Medical Imaging, Ingolstädter Landstrasse 1, Neuherberg 85764, Germany. Tel: +49 89 3187 3852; Fax: +49 89 3187 3017; E-mail: v.ntziachristos@tum.de

In addition to intrinsic contrast, the use of fluorescent dyes and probes has been also proposed to offer diagnostic information on the inflamed synovial tissue based on planar and tomographic molecular imaging techniques.^{22,23} Optical imaging employing indocyanine green (ICG) has been considered in particular for visualizing RA in preclinical and clinical applications.^{9,12,24–26} ICG is a synthetic organic fluorescent dye that has been considered in a variety of clinical applications, including hepatic clearance studies and retinal angiography, as well as intraoperative applications such as brain surgery and gastroenterological surgery.^{27–31} Studies for the detection of breast cancer^{32,33} and the identification of atherosclerosis³⁴ have also been considered. Upon intravenous administration, ICG distributes into the vascular system, typically binding to plasma proteins. ICG has a half-life of 3 to 4 min after injection and clears through the hepatobiliary tract. ICG has peak optical absorption at ~780 nm and peak fluorescence at 830 nm in blood.³⁵

A common method to clinically visualize ICG using optical imaging is epi-illumination fluorescence imaging (EFI), i.e., a photographic approach whereby the illumination and the detection are placed on the same side of tissue.^{14,36–38} Transillumination and optical tomography imaging have, however, also been demonstrated.^{39,40} When performing EFI, the sample is typically subjected to plane illumination and the fluorescence signal is measured using a CCD at the corresponding wavelength using appropriate optical filters that reject the excitation light and only allow the emission light to be detected. Such cameras can operate at video rates, allowing dynamic measurement of fluorophore biodistribution. Conversely, the approach is surface weighted, which means that fluorescence coming from the surface of the tissue is collected more efficiently than deeper-seated fluorescence which is instead attenuated as a function of depth. It should be noted that, to our knowledge, ICG-based EFI imaging as proposed in Ref. 24 is to date the only fluorescence-based clinical tool for imaging synovitis in human hand joints and at the same time the only technique for simultaneously imaging synovitis in all carpal, MCP, and interphalangeal joints of the human hand. ICG-aided diagnosis of RA in carpal, MCP, PIP, and DIP joints of human hands was reported in Ref. 41 to have a sensitivity of 39.6% and specificity of 85.2% in a group of 45 patients. Another study reported 76% sensitivity and 54% specificity for 252 patients.²⁶

The output of EFI imaging is a number of fluorescence frames obtained at sequential time points. The visual inspection of this information and derivation of diagnostic information is not straightforward due to the large amount of data collected and perhaps the presence of subtle spatiotemporal changes that are not easily captured by human perception. In order to quantitatively examine the ICG spatiotemporal profile obtained from clinical measurements following an intravenous bolus injection of ICG to patients, we employed principal component analysis (PCA).⁴² PCA is commonly applied in studying dynamic events and has been used in such applications as differentiating internal organs in mice,³⁷ spectral unmixing applications,⁴³ and multi-spectral optoacoustic tomography real-time imaging.⁴⁴ PCA was applied herein to decompose the complex temporal and spatial dependencies of fluorescence signals following ICG administration and investigate whether we could identify dynamic or spatial patterns associated with RA. A secondary objective of this work was to further gain insights on the effects of depth on the signals recorded. The purpose of the spatiotemporal

processing was to investigate whether ICG of higher concentration or different time-kinetics was delivered at the synovial lining compared to the surrounding tissue, as this could be employed as a marker of RA characterization. A numerical phantom model built using a manually segmented MR scan of an MCP joint has been used to simulate the fluorescence image sequences based on the finite element method (FEM). The performance of the proposed method has been demonstrated using this phantom as well as for individual joints from 10 patients diagnosed with RA and 5 healthy volunteers. Detailed case studies are presented as well for eight joints with various degrees of synovitis severity.

2 Methods

2.1 Clinical Imaging of Rheumatoid Arthritis

The methodology and analysis performed in this paper has been developed in the context of a recent study conducted at the Klinikum Rechts der Isar, Munich, Germany, with the purpose of evaluating ICG-aided diagnosis of RA.⁴¹ Patients with more than one tender and/or swollen joint among carpal, MCP, PIP, or DIP joints were recruited, when the symptom duration exceeded 6 weeks for up to 24 months. The patients were examined by two rheumatologists via bimanual palpation and then underwent imaging using a 3T MR machine (Verio, Siemens Erlangen, Germany). The MR scanning was performed on both hands simultaneously with patients in a prone position and hands stretched out in praying posture. Gadopentetate dimeglumine (Magnevist, Schering, Berlin, Germany) was injected as contrast agent at a dose of 0.02 ml per kg body weight. Nonenhanced proton density fat-saturated images and postcontrast T₁-weighted fat-saturated scans were obtained in transverse and coronal planes. The contrast agent shows a higher relative concentration in inflamed than healthy synovial joint linings.⁴¹ Three radiologists scored the degree of synovitis in a total of 30 joints of both hands using the MR scans. Synovitis scores on a 4-point-ordinate scale (0: no inflammation, 1: mild, 2: moderate, 3: severe) were assigned to each joint according to the semi-quantitative assessment system suggested by the OMERACT MRI group.⁴⁵ These MR scores constitute the diagnostic information for our work.

Figure 1 shows characteristic images for a patient with mild (MR score of 1) arthritis in the third MCP joint of the left hand. The bright area around the third MCP joint region, marked in Fig. 1(b), indicates relatively high accumulation of ICG in the synovial membrane of this joint. The corresponding transverse MR image is shown in Fig. 1(c), where the synovitis is visible as hyperintense signal alteration on T₁-weighted, fat-saturated, contrast-enhanced MR images due to the higher concentration of the MR contrast agent. The regions of interest (ROIs) delineated with white lines in Fig. 1(c) are manually specified for each patient and are used in the proposed method, presented in Sec. 2.2.

Fluorescence imaging was performed with a near-infrared fluorescence imaging system (Xiralite X4, Mivenion GmbH, Berlin, Germany), which allows for real-time image acquisition at the fluorescence wavelength of ICG from the human hands after epi-illumination excitation.^{24,26,41} The device employs a cooled CCD camera, equipped with an 800-nm long-pass optical filter, which captured images at a frame rate of one image per second for a total duration of 360 s. For optical imaging, the patient placed the hands inside the device, on a template

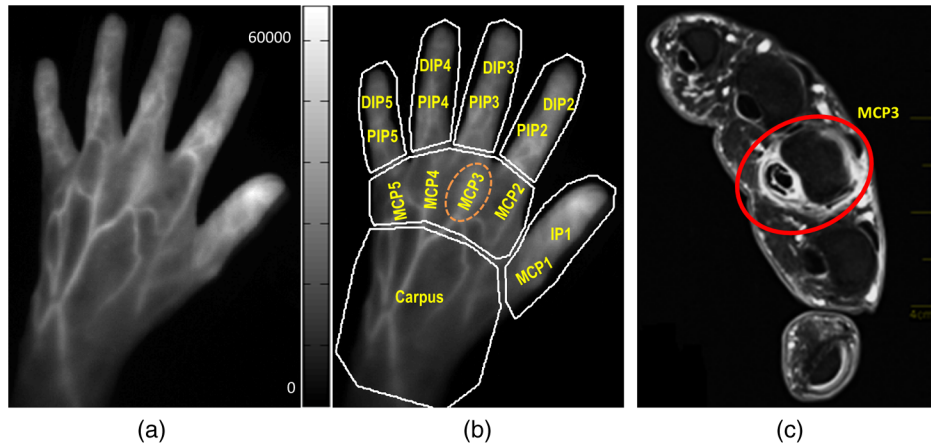


Fig. 1 (a) Sample epi-illumination fluorescence image of the left hand 40 s after injection of indocyanine green (ICG). The patient has mild synovitis in the third metacarpophalangeal joint of the left hand, as seen by relative signal increase in the delineated region. (b) The joint names are indicated on the fluorescence image (MCP, metacarpophalangeal, PIP, proximal interphalangeal, and DIP, distal interphalangeal). White curves depict regions of interest (ROIs) specified for processing purposes. (c) The corresponding contrast enhanced, fat saturated, T_1 -weighted magnetic resonance (MR) image of the MCP region where the synovitis in the third MCP joint is highlighted due to a higher relative concentration of the MR contrast agent.

designed to keep the fingers apart. Continuous illumination with light-emitting diodes at 740 nm was applied to both hands. The patients received a bolus injection at a dosage of 0.1 mg per kg body weight. ICG was injected intravenously approximately 10 s after the beginning of the imaging acquisition so that pre-ICG administration baseline measurements were always available.

2.2 Fluorescence Image Analysis

To analyze the fluorescence data collected, PCA was employed to decouple the fluorescence image sequence into different temporal and spatial components. PCA is a method for converting a set of realizations of a group of random variables to a smaller set of values, which can be considered as realizations of a corresponding group of uncorrelated random variables, known as principal components.⁴² PCA was applied to a temporally and spatially windowed subsequence of the original raw fluorescence image sequence measured from patients' hands as described in Sec. 2.1. The resulting principal components in each subsequence were then combined to form another sequence. This new sequence was efficiently rendered as a sequence of color images, where each color corresponds to a principal component. The signal due to synovitis is likely to appear as one of such components if it has a dynamic behavior that differs from that of regular tissue.

The proposed processing method achieves signal separation through multiple levels of localization in time and space. In the first step, the hand image is divided into various ROIs as shown in Fig. 1(b). There are seven ROIs considered for different regions of the hand. This step is necessary as the signals have different temporal and spatial characteristics in various hand regions due to different vascular and anatomical structures and, therefore, hemodynamics. For example, there is a denser dorsal venous network in the digital (consisting of PIP and DIP ROIs) compared to the carpal joints, contributing to more signal interference in interphalangeal joints. Similarly, the synovial tissue regions in the MCP joints are shallower and smaller than the carpal synovium and, therefore, appear as better defined yet smaller spots in the fluorescence images compared to the signal coming from inflamed carpal joints. These

observations necessitate localized processing as the processing method seeks component separation through minimization of spatial and temporal correlations. The processing is best focused on regions with similar signal dynamics. Hence, joints with similar signal behavior are processed in one ROI.

To briefly explain the application of PCA herein, we can assume $\{J_p\}$, $p = 1 \cdots P$, as a set of P fluorescence images of $M_1 \times M_2$ pixel size, obtained correspondingly at P time points. In our study, P was equal to 360, corresponding to 360 images acquired over 360 s. Then for a given joint, let $\{J_p\}$, $p = 1 \cdots P$ denote the sequence of cropped images at the corresponding ROI, as shown in Fig. 1(b). The average intensity within each ROI was subtracted from this image sequence, such as each J_p had a mean value of zero. Just as the spatial windowing through the application of the ROI windows is conducive to better performance, the windowing across the time domain also leads to better signal separation, due to changes in hemodynamic characteristics postinjection. Specifically, L successive images were taken from the subsequence J_p and weighted using a time window that tapered off toward the boundaries of this subsequence. Assuming that this subsequence is H_i^k , where i ranges from 1 to L and k ranges from 1 to $P - L$, we then write

$$H_i^k = W(i)J_{k+i}, \quad (1)$$

where W denotes the window sequence. The window's length, L , was empirically adjusted such that the L images within the time window W have a stationary spatiotemporal behavior, that is, can be well approximated as linear combinations of few spatial components. For the work presented here, a triangular window of varying length was employed. The length of the window W was shorter at the beginning of the sequence, where the temporal dynamism was stronger, and became longer as signal later stabilized. The sequence H_i^k was the image sequence that was finally processed by PCA.

To implement the PCA on H_i^k , every image in the sequence H_i^k was first vectorized by tagging along all the columns, i.e.,

$$h_i^k = [H_i^k(1, 1) \cdots H_i^k(M_1, 1) \cdots H_i^k(1, M_2) \cdots H_i^k(M_1, M_2)], \quad (2)$$

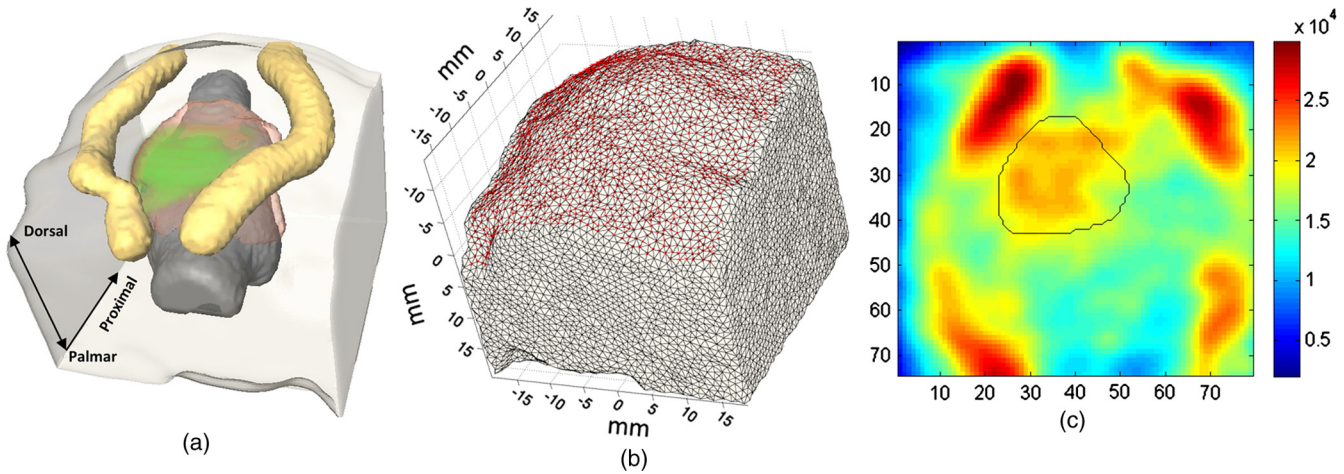


Fig. 2 Numerical tissue phantom built using segmentation of transverse MR images of an MCP finger joint: (a) The phantom contains general tissue, two dorsal veins (yellow isosurfaces), bones (gray isosurface), and synovium (red isosurface), and ICG accumulated in the synovium is shown by the green shade. (b) Tetrahedral mesh generated for the numerical phantom with the red dots designating the illumination on the surface. (c) A sample simulated fluorescence image (as seen by a camera located above the hand and seeing the dorsal side) for synovium located at the depth of 2 mm with an uptake ratio of 3 relative to general tissue, with the black curve delineating the joint region. The units in (c) are pixel intensity counts.

where $H_i^k(n, m)$ is the n 'th row and m 'th column element of the matrix H_i^k . For a given k , all the images in the sequence H_i^k were vectorized and stacked on top of each other to form an $L \times M_1 M_2$ matrix \mathbf{X}_k as

$$\mathbf{X}_k = \begin{bmatrix} h_1^k \\ \vdots \\ h_L^k \end{bmatrix}. \quad (3)$$

The PCA transformation on this matrix relied on the singular value analysis of the $L \times L$ correlation matrix \mathbf{C}_k defined as

$$\mathbf{C}_k = \mathbf{X}_k \mathbf{X}_k^T = \mathbf{T}_k^T \mathbf{D} \mathbf{T}_k, \quad (4)$$

where the $L \times L$ unitary matrix \mathbf{T}_k is the matrix of eigenvectors of \mathbf{C}_k and \mathbf{T} is the matrix transpose operator. The diagonal matrix \mathbf{D} contains the eigenvalues of \mathbf{C}_k , i.e., the squares of singular values of \mathbf{X}_k sorted in decreasing order. The PCA transformation of matrix \mathbf{X}_k is then given by

$$\mathbf{S}_k = \mathbf{T}_k^T \mathbf{X}_k, \quad (5)$$

where \mathbf{T}_k and \mathbf{S}_k are $L \times L$ and $L \times M_1 M_2$, respectively. It was observed that only the first three components had significant energy, and the components beyond the third one could be ignored. In other words,

$$\mathbf{X}_k \cong \hat{\mathbf{T}}_k \hat{\mathbf{S}}_k, \quad (6)$$

where $\hat{\mathbf{T}}_k$ and $\hat{\mathbf{S}}_k$ are matrices containing the first three, respectively, columns and rows of matrices \mathbf{T}_k and \mathbf{S}_k . The values of the time profile and the spatial components, respectively in $\hat{\mathbf{T}}_k$ and $\hat{\mathbf{S}}_k$ matrices, may become negative as the PCA transformation does not enforce non-negativity. The negative values pose a problem for result interpretation. For this reason, the three imaging components were weighed by the corresponding values of the temporal vectors and thresholds were applied using preset positive numbers. The corresponding three PCA component sequences are called $\{C_i^1\}$, $\{C_i^2\}$, and $\{C_i^3\}$. For each window

position, the three components from the middle frame weighed as such are then mapped into the blue, red, and green transparency channels of a color image in decreasing order of the amplitude of their corresponding singular values. The resulting color image is considered as a single frame in a video sequence, which is finally presented to the reader. It should also be noted that all frames are normalized across the entire sequence for a more meaningful depiction.

2.3 Simulation and Analysis Using the Finite Element Method

To justify the use of superficial measurements for recovering diagnostic information from deeper-seated activity as well as studying the performance of the proposed PCA method, we simulated the fluorescence signals recorded as a function of assumed physical and geometrical factors that relate to the imaging problem studied herein. The simulated factors include the depth and estimates of the relative ICG uptake ratio of the synovial linings. We have furthermore investigated the visibility of the targeted fluorescence signal in various time stages as the ICG is distributed through the hand and joint area.

Figure 2 demonstrates the numerical phantom model that was developed and used for the above purposes. The phantom geometry was developed using manual segmentation of transverse MR images of an MCP joint of a patient with severe synovitis in the second MCP joint. Three elements were identified in the segmentation—bone, veins, and synovium—as shown by different colors in Fig. 2(a). The ICG was assumed to accumulate in both the background tissue (volume outside of bones) and in the synovium at different concentrations. In particular, it was assumed that the concentration of the fluorophores in the inclusion and the background, i.e., the rest of the slab, constitutes an uptake ratio of $N:1$. To estimate the dynamic range of the uptake ratio N , we measured intensity of fluorescence observed in several inflamed joints relative to signal in adjacent nonjoint tissue. In the measured samples, the joint to nonjoint fluorescence ratios ranged between 2.5 and 6.0. While these measured ratios depend on many physical factors such as the imaging time point or the location, the extracted dynamic range serves as an

estimate of the underlying uptake ratio. Because of higher attenuation of deep-seated inflammation signal due to depth effects, this estimate is likely to be a conservative one. Interestingly, intensity of the inflamed synovium was observed in MR images to be, depending on severity of inflammation, two to seven times larger than surrounding tissue. This is justifiable as the gadolinium-based MR contrast agent and ICG are both blood pooling agents and the respective signal intensities are expected to correlate with blood concentration, even though they have different distribution patterns due to their different molecular weights. This effect has also been observed in ICG-based mammography.⁴⁶

The ICG that accumulated in the synovium is shown by green shade in Fig. 2(a) and corresponding N -fold increased fluorophore concentration in the target tissue (synovium), with regard to background, as described above. An FEM model was employed to simulate the propagation of the incident light and calculate the light intensity emitted by fluorophores for a given ICG distribution. The mesh consisted of 48,880 nodes and 278,832 elements, with an average edge length of 1.3 mm, and was generated using the methods described in Refs. 47 and 48. The light propagation in tissue was modeled using FEM-based discretization of the diffusion approximation (DA).⁴⁹ The DA, as a first-order approximation of the more general radiative transport equation (RTE), is valid for modeling light propagation in turbid tissue where the scattering coefficient is much larger than the absorption coefficient. In tissues, this optical condition does not generally hold in regions containing clear fluid such as the synovium or air such as in the lungs, or in regions with very high absorption such as within large blood vessels. Nevertheless, light modeling based on DA is widely used for preclinical applications (such as tumor localization in murine models of lung cancer⁵⁰) and clinical applications, including tomographic imaging of human interphalangeal finger joints^{17,51,52} as well as for simulation of light propagation in joints.⁷ RTE and its higher-order approximations are employed as well as a more accurate model for tomographic imaging of finger joints, but computational particulars also impose a number of approximations and assumptions.^{15,53} A recent study showed that, given *a priori* anatomical information obtained through x-ray imaging, the DA-based modeling of light propagation results in <4% error tomographic reconstruction in human joints, in comparison with higher-order approximations of RTE, while without such *a priori* information, the reconstruction error can be significantly larger.⁵³ The tissue's optical absorption and scattering coefficients were set to typical values of 0.05 mm^{-1} and 1.0 mm^{-1} , typical for tissue. Figure 2(b) shows the tetrahedral mesh generated for the phantom, and the red dots mark the illumination surface. Figure 2(c) depicts a sample fluorescence image obtained using the FEM modeling.

Dynamic fluorescence images were simulated over 360 s by assigning time-dependent ICG concentrations to different tissue segments. Specifically, the blood flow was mimicked by weighting the ICG concentration in the background, veins, and synovium according to time courses experimentally obtained from fluorescence measurements from the patient whose MR scan was used for the phantom construction. Three time-curves were measured from three different locations, i.e., the dorsal vein, general tissue, and inflamed joint locations. The final simulated image sequence contains the fluorescence signal emanating from different entities in the phantom and an added

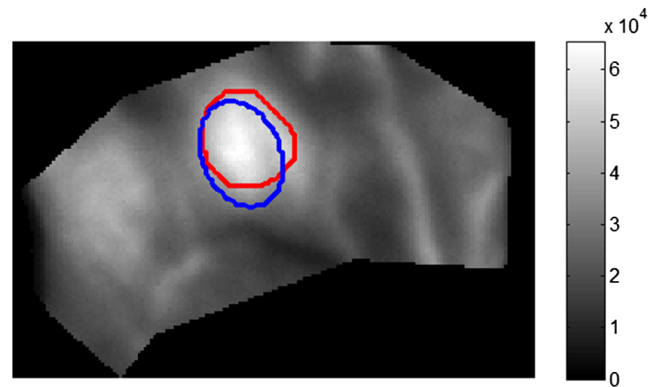


Fig. 3 Fluorescence image in the MCP area of a patient with moderate synovitis in the second right MCP joint. The blue ellipse shows the region the joint is located, i.e., the reference joint region, and the red curve designates the segmented region that best overlaps with the reference joint region.

Gaussian measurement noise with 1.5% of the fluorescence signal energy.

2.4 Localization Metric for Image Evaluation

In this section, we establish a framework for quantitative evaluation of the results and comparison of raw and processed component image sequences. This framework is then used to evaluate the performance of the proposed method in localizing desirable signal components in both FEM-based simulated and clinical fluorescence image sequences. The idea behind such framework is to quantify the presence of a component in an image, which can be potentially attributed to the target fluorescence source, i.e., in our case, the synovitis signal. This is achieved by segmentation of the image and then evaluation of the binary segments against a reference binary image. The reference binary image is manually set to a region where the joint is expected (for clinical images, this region was set with the help of MR coronal images). If an image segment is localized to the region denoted by the reference binary image, it can be potentially associated with the fluorescence signal emanating from joint synovitis.

Specifically, given an image sequence, raw or processed, and an ROI where a joint is expected to be located, a localization metric was designed whose value indicates if the image sequence suggests the existence of a localized signal component in the joint region. This metric has a value between 0 and 100, where a value of 100 suggests existence of a signal component confined within and spanning the joint region and 0 suggests no localized signal component in the joint region. This metric is applied on every image in the sequence and the metric associated with the image sequence is defined as the maximum of all metrics for the images in the sequence. Hence, the image with the maximum metric value is regarded as the one containing the best candidate signal component. For clarification purposes, an example is presented in Fig. 3. The blue ellipse delineated in Fig. 3 denotes the approximated location of the second MCP joint, defined as the “joint ROI.” The fluorescence signal emanating from the ICG accumulated in the inflamed synovial lining is expected to appear as a distinguishable and localized signal component at least partly within the joint ROI. The fluorescence image in Fig. 3 contains such a component, delineated by the red

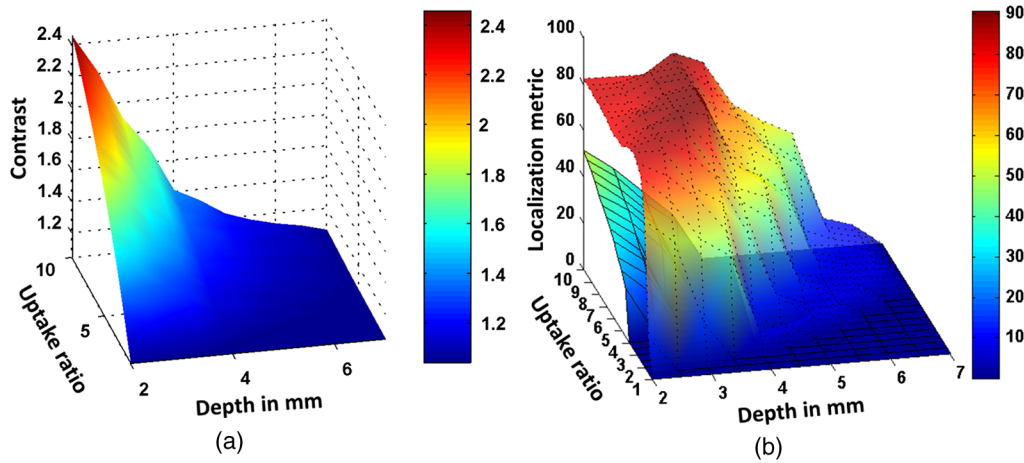


Fig. 4 Simulation and processing results for the numerical phantom presented in Fig. 2, Sec. 2.3. (a) The ratio between the signal intensities in the joint ROI and in the background for various depths of the synovium and ICG uptake ratio in the synovium, calculated for the simulated raw fluorescence image sequence (contrast denotes the maximum of this ratio over the entire sequence). (b) Localization metric for the raw simulated fluorescence sequences (surface marked with solid lines) and for the three processed image sequences corresponding to the three components (surface marked with dotted lines) versus depths and uptake ratios. A higher value for the localization metric indicates presence of a localized component in the joint region in the corresponding image sequence.

curve. This component has been segmented using the segmentation approach of the metric framework proposed in the section.

Specifically, let R denote a binary image that is 1 inside the joint region and 0 outside. For a given image I of size $N \times M$, a binary image J is constructed as follows:

$$J = I > \beta I_0, \quad (7)$$

where I_0 indicates the average intensity of I and the coefficient β was heuristically set to 1.5 for the fluorescence images I obtained from patients' hands as described in Sec. 2.1. The binary image J is further processed using morphological operations. Finally, a connected component, also called a binary label, of the resulting binary image that has the largest overlap with R is kept as the candidate signal component. Let K be the binary image containing this segment.

The similarity between the reference binary images R and the segmented binary image K renders a measure of the likelihood of the signal component designated by the binary region in K , to have been originated from fluorescence within the region designated by R . To quantify the similarity between R and K , we employ the Jaccard distance⁵⁴ as an overlap-based measure and the Hausdorff distance⁵⁵ as a boundary-based measure and the signal energy. The application of Hausdorff and Jaccard distances as typical boundary-based and overlap-based localization metrics is a common approach for segmentation and image retrieval evaluation purposes.⁵⁶⁻⁶⁰ A survey and comparison of several localization metrics for the purpose of evaluation of image interpretation systems is presented in Ref. 61.

Specifically, in this work, the localization metric for a binary image K , a given reference binary image R , and the original gray-scale image I is defined as

$$S(K, R) = 100 \times \left(1 - \max \left\{ \frac{\max[d(K, R), r]}{r}, J_\delta(K, R), 1 - E(K) \right\} \right), \quad (8)$$

where $d(K, R)$ and $J_\delta(K, R)$ denote, respectively, the Hausdorff distance and the Jaccard distance between K and R , and $E(K)$ is

the energy of the image I within the label in K normalized by the energy of the image I . The number r denotes the major radius of an ellipse that envelopes R . $S(K, R)$ ranges between 0 and 100. The configuration of Eq. (8) ensures that a high value of $S(K, R)$ means small Hausdorff and Jaccard distances and a high energy concentration within the segmented region. Specifically, $S(K, R) = 100$ means that the K and R are identical and that the entire signal energy is confined to K , i.e., perfect localization. On the other hand, a value of 0 for $S(K, R)$ indicates no overlap or a large Hausdorff distance between K and R or no signal energy contained within the area defined by K .

The metric for a given image sequence I_i is defined as

$$S(\{I_i\}, R) = \max_i S(I_i, R). \quad (9)$$

The metric proposed here is used in Sec. 3 for two purposes. First, it is employed to compare the processed component sequences against the draw image sequence for various joints with different degrees of synovitis severity. Second, the metric is used to study the performance of the method versus different physical factors such as lesion depth and uptake ratio using the numerical phantom presented above in Sec. 2.3.

3 Results

3.1 Processing of FEM-Based Simulated Image Sequences and Impact of Physical Factors

In this section, we establish the impact of physical and geometrical parameters, such as the synovium depth or the concentration of the ICG in the synovium, on the fluorescence signal obtained for the geometrical arrangement presented in Sec. 2.3. Figure 4(a) demonstrates results from the numerical phantom study. The FEM-based model discussed in Sec. 2.3 was used to simulate the propagation of incident planar illumination in the tissue and the resulting fluorescence signal emanating from the synovial inclusion, the background tissue, and the veins. The z axis in Fig. 4(a) denotes the relative contrast between the fluorescence signal in the joint region, as shown in Fig. 2(c), and the background signal in the simulated images for different depths

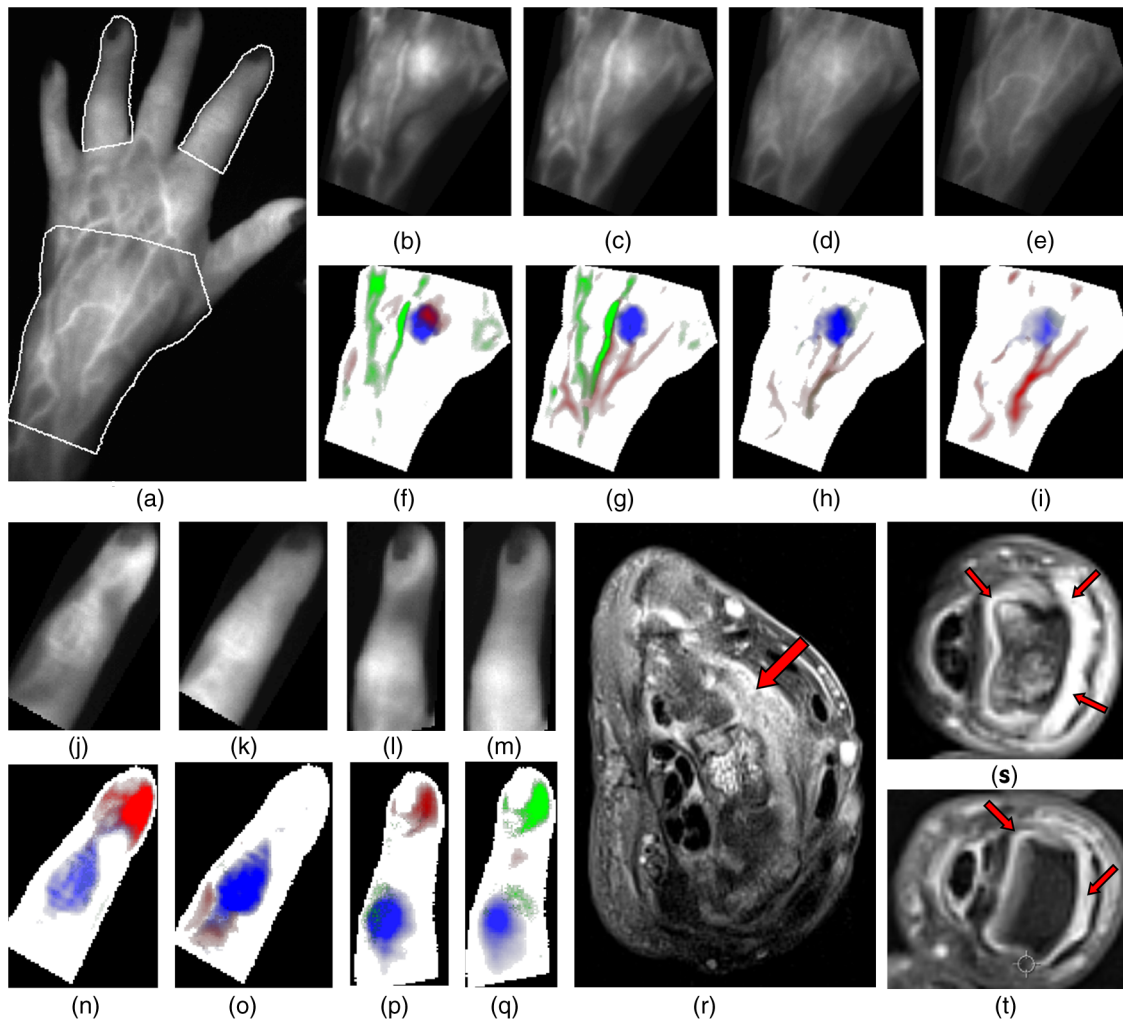


Fig. 5 Case study of a 64-year-old female patient with severe synovitis in the left carpus and severe and moderate synovitis in, respectively, left second and fourth PIP joints. (a) Sample fluorescence image at 100 s with corresponding three ROIs delineated by white curves. (b) to (e) Raw fluorescence images (0 to 65,535 intensity counts with black indicating 0) corresponding to time points 37, 43, 53, and 89 s postinjection, respectively; (f) to (i) Corresponding processed colored images at the same four time points. (j) to (k) and (n) and (o) are raw and processed images for the left second PIP, and (l) and (m) and (p) and (q) correspond to the results for the left fourth PIP joint for time points 30 and 42 s postinjection. The inflamed synovial linings characterized by higher relative accumulation of MR contrast agent are marked on transverse contrast-enhanced T1-weighted MR images in (r) to (t) for left carpus and second and fourth PIP joints, respectively. The three principal components are mapped to red, green, and blue channels in (f) to (i) and (n) to (q). In all cases and time points shown, the signal in the blue channel signifies synovitis, while green and red channel signals can be mainly attributed to fluorescence emanating from dorsal veins in (f) to (i) and the dense vascular network of fingertips in (n) to (q).

between 2 and 7 mm and uptake ratios between 1 and 10, whereby uptake ratio denotes ratio of ICG concentration in synovium over the background. Figure 4(b) illustrates the results obtained from a simulated longitudinal measurement. Specifically, for each depth and uptake ratio, the proposed PCA-based method was applied to the raw fluorescence image sequence generated using the numerical phantom, where different frames denote the simulated fluorescence signal intensity images over 360 s, as elaborated in Sec. 2.4. Next, localization metric values for the simulated raw image sequences as well as the corresponding processed sequences were found, as shown in Eq. (9). The localization metric was calculated for the individual simulated images based on the approach described in Sec. 2.4 and Eq. (8). The z axis in Fig. 4(b) denotes the value of the localization metric calculated for different depths and uptake ratios for both the raw image sequences (surface marked with solid lines) and the processed sequences (surface marked with dotted lines). A high value for the localization metric indicates

presence of a signal component attributable to the synovium fluorescence.

The results suggest that fluorescence signals can be retrieved for depths where synovitis can occur for different joints. In addition, the PCA analysis shows the presence of a signal component localized in the joint region for larger range of uptake ratios and a given depth and vice versa. The fluorescence signal in finger joints is also affected by the impact of the blood flow on the ICG distribution. After the intravenous injection, the ICG circulates to the hands through the radial and ulnar arteries and then flows back through palmar and venous veins, resulting in fluorescence signal emanating from dorsal veins and general tissue interfering with the synovitis signal. The FEM simulations presented in Fig. 4(a) suggest that even for synovitis up to 3 mm under skin, interference occurring for uptake ratios <3 can complicate signal detection. However, as seen in Fig. 4(b), the PCA-based method could decouple the fluorescence signals from the vein and background signal for the

Table 1 Localization metric values calculated for raw and processed image sequences for cases presented in Figs. 5 to 8.

	MR score	Sequence localization metric		Channel with maximum localization
		Raw	Processed	
Left carpus, Fig. 5	3	35	83	1 (blue)
Left second proximal interphalangeal (PIP), Fig. 5	3	0	66	1 (blue)
Left fourth PIP, Fig. 5	2	0	46	1 (blue)
Right third metacarpophalangeal (MCP), Fig. 6	3	31	60	1 (blue)
Left carpus, Fig. 7	2	0	32	2 (red)
Left second MCP, Fig. 7	2	0	54	2 (red)
Left third MCP, Fig. 7	1	0	48	2 (red)
Left fourth MCP, Fig. 7	2	0	8	3 (green)
Left fifth MCP, Fig. 7	2	0	9	3 (green)
Right carpus, Fig. 8	0	0	0	—

Note: Columns 1 through 5 indicate, respectively, the joint name and location, the MR-based synovitis score, the localization metric values for raw and processed sequences, and the channel where the frame with the maximum metric occurs.

FEM-based time-series simulations for lesions up to 5 mm deep for uptake ratios <5 , while the target signal could be distinguished in the raw fluorescence images only up to 2 mm of depth.

3.2 Spatiotemporal Analysis Applied to Arthritic Hand Joint Images

Following the analysis of simulated data, we applied the PCA method in the study of RA patients. Figure 5 shows raw and processed results for a fluorescence image sequence obtained from a 64-year-old female patient with severe arthritis in the left carpus and moderate and severe synovitis in, respectively, left fourth and second PIP joints. The ROI of these three joints of the left hand are delineated in Fig. 5(a). Transverse T_1 -weighted contrast-enhanced fat-saturated MR images verifying the synovitis severity of left carpus and second and fourth PIP joints for this patient are also shown in Figs. 5(r) to 5(t), respectively. The raw fluorescence images measured at time points 37, 43, 53, and 89 s are shown in, respectively, Figs. 5(b) to 5(e) within the ROI corresponding to the carpus joint. Figures 5(f) to 5(i) show the corresponding processed images at these time points, where the three components are mapped, according to increasing magnitude of the corresponding singular values, to the green, red, and blue channels of depicted color images. The color values in processed images range between 0 and 1. A prominent fluorescence signal appears on the raw images of the carpus, in particular at time point 37 s. Accordingly, a strong first PCA component (mapped to the blue channel) appears in Figs. 5(f) to 5(i), congruent to the location where the fluorescence signal appears in the raw data. Interestingly, component #1 appears in all time points of the sequence, in contrast to the raw fluorescence signal that virtually disappeared at later time points as shown in Figs. 5(d) and 5(e). The raw and processed image frames for the left second PIP joint are shown in Figs. 5(j) and 5(k) and Figs. 5(n) and 5(o), respectively, and

Figs. 5(l) and 5(m) and Figs. 5(p) and 5(q) present corresponding results for the left fourth PIP joint for time points 30 and 42 s postinjection. Similar to the carpus, a strongly localized signal component appears in the first component, visible in the two time-point displays for both joints.

The severe synovitis of the left carpal and second PIP joints as well as the moderate synovitis of fourth PIP joint can be easily seen in the blue channel of the processed images. This example demonstrates the virtue of the proposed method in temporal and spatial decoupling of the various signal components contributing to the fluorescence image. Specifically, the signal from the veins and the synovitis are clearly decoupled into the three color channels (corresponding to the three principal components) in Fig. 5(g) for the carpus, at the time point 24 s. The synovitis signal is the most temporally persistent component (in comparison with the vein signals, for instance). It is therefore transformed into the blue channel, which is the most dominant channel, i.e., with the largest singular value. On the other hand, the vein signal passes through the green and red channels at different time points. Some of the synovitis signal has leaked as well into the red channel, as seen in Fig. 5(f). The localization metric calculated for raw and processed image sequences were calculated according to Eq. (9). The reference ROIs for the three joints in this and next cases were set using the fluorescence images and the corresponding MR coronal images, as the anatomical reference. The metric values for these joints and other joints studied in this section are presented in Table 1. The metric for the processed sequence represents the maximum of the three sequences, corresponding to the three components. As can be seen, the first component (mapped to blue channel) in the processed sequence achieves a maximum metric of 83 for the carpus, while the corresponding value for the raw sequences is 35. For the second and fourth PIP joints of the left hand, metric values of, respectively, 66 and 46 were calculated for the processed sequences, while no localized components were found in the

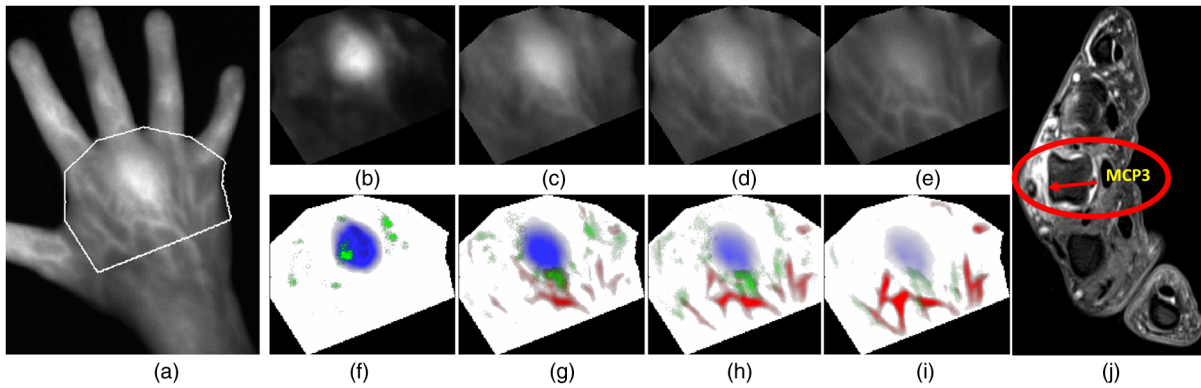


Fig. 6 Case study of a 46-year-old female patient with severe synovitis in the third right MCP joint. (a) Sample fluorescence image at 100 s with MCP ROI delineated by white line. (b) to (e) Raw fluorescence images corresponding to time points 35, 57, 67, and 91 s postinjection, respectively. (f) to (i) Corresponding processed colored images at the same four time points. (j) A transverse contrast-enhanced T_1 -weighted fat-saturated MR image of the MCP joints with the red arrow depicting the inflamed synovial lining characterized by higher relative accumulation of MR contrast agent. The three principal components are mapped to red, green, and blue channels in (f) to (i). The signal in the blue channel signifies synovitis in the third MCP at all four time points. The green and red channel signals can be attributed to background and vein signal, respectively.

raw images, leading to a metric value of 0. This is likely due to the strong coupling of synovitis signal with the signal from non-specific background and dorsal venous networks of fingers.

Another presentation for a severely arthritic joint presented in Fig. 6 further demonstrates the decoupling ability of the proposed method. In this case, a 46-year-old female patient with severe synovitis in the third right MCP joint is presented. The raw fluorescence images in the MCP region, as delineated in Fig. 6(a), are shown in Figs. 6(b) to 6(e) at time points 35, 57, 67, and 91 s after ICG injection. The corresponding processed images are shown in Figs. 6(f) to 6(i). As in the previous case, a strong fluorescence signal appeared in this case as well in the raw fluorescence images at the MCP second region. This signal is stronger at earlier time points and later weakens. Correspondingly, the first PCA component showed a strong signal that similarly diminished with time. A transverse MR image of the right MCP joints of this patient is shown in Fig. 6(j), which verifies an area with apparent severe synovitis at the third right MCP joint. Due to its strength and temporal persistence, the synovitis signal also shows up in the blue channel here and the vein signal mostly in the red channel. There is very little contribution in the green channel. Similar to the previous case, the inflammation signal is well decoupled from the background in the last time point, while fairly unclear in the raw fluorescence image. The metric values for this case, as seen from Table 1, are 31 and 60 for, respectively, the raw and the blue channel of the processed sequence.

The cases presented in Figs. 5 and 6 corresponded to carpal, MCP, and PIP joints with moderate to severe synovitis. The proposed method is also applied to joints with mild to moderate synovitis. As described in Sec. 2.1, the joints with mild and moderate synovitis correspond to MR-assigned synovitis scores of 1 and 2, respectively.

The processing results for a 49-year-old female patient with mild to moderate joint synovitis are presented in Fig. 7. The processing results are shown for two ROIs—the carpus ROI and the MCP ROI—as shown in Fig. 7(a). Transverse images of the MCP region and image of the carpus, as shown in Figs. 7(h) and 7(i) and Figs. 7(r) and 7(s), respectively, present the MR findings for this patient with the red arrows depicting synovitis. The patient suffers moderate synovitis in the third

right MCP and the left carpal joints and mild synovitis in the second right MCP joint.

Figures 7(b) to 7(d) and Figs. 7(e) to 7(g) demonstrate the raw fluorescence images and the processed images corresponding to the time points 37, 52, and 99 for the MCP region. This patient had mild synovitis in the third MCP joint and moderate synovitis in the second, fourth, and fifth MCP joints. While almost invisible and indistinguishable in the raw fluorescence images, the synovitis signals are clearly seen in the marked locations in Figs. 7(f) and 7(g). Furthermore, the raw fluorescence images for time points 37, 48, 72, and 99 and the corresponding processed images for the carpus are shown in Figs. 7(j) to 7(m) and Figs. 7(n) and 7(q), respectively. The signal from carpus synovitis is almost invisible in the raw fluorescence images, i.e., Figs. 7(j) to 7(m). However, the red channel shows a transient signal component in Fig. 7(q) inside the marked region, which can be potentially attributed to the inflammation in the carpus. The vein signal appears in the red and green channels transiently in Figs. 7(n) to 7(q) and persistently in the blue channel across all four time points. As seen in Table 1, the localization metric values for the second and third MCP joints reach a maximum of, respectively, 54 and 48 in the red channel and 0 in the raw sequence. The corresponding metric values for the carpus are 32 and 0 for the red channel of the processed sequence and the raw sequence, respectively. It should be mentioned that although the patient was diagnosed based on MR to have moderate synovitis in both fourth and fifth left MCP joints, both raw and processed sequences achieve very low (0 and 8, respectively) metric values, which means the inflammation was not detectable in either sequence.

3.3 Spatiotemporal Analysis Applied to Healthy Hand Joint Images

Figure 8 demonstrates a control case of a 43-year-old male patient with no inflammation in the right carpus. The raw fluorescence and processed images are shown in Fig. 8 for the carpus ROI, delineated in Fig. 8(a) for a sample fluorescence image at time point 100 s. Specifically, Figs. 8(b) to 8(d) depict the cropped raw fluorescence images obtained at time points 36, 42, and 61 s postinjection, and Figs. 8(e) to 8(g) show the corresponding processed images consisting of the three PCA

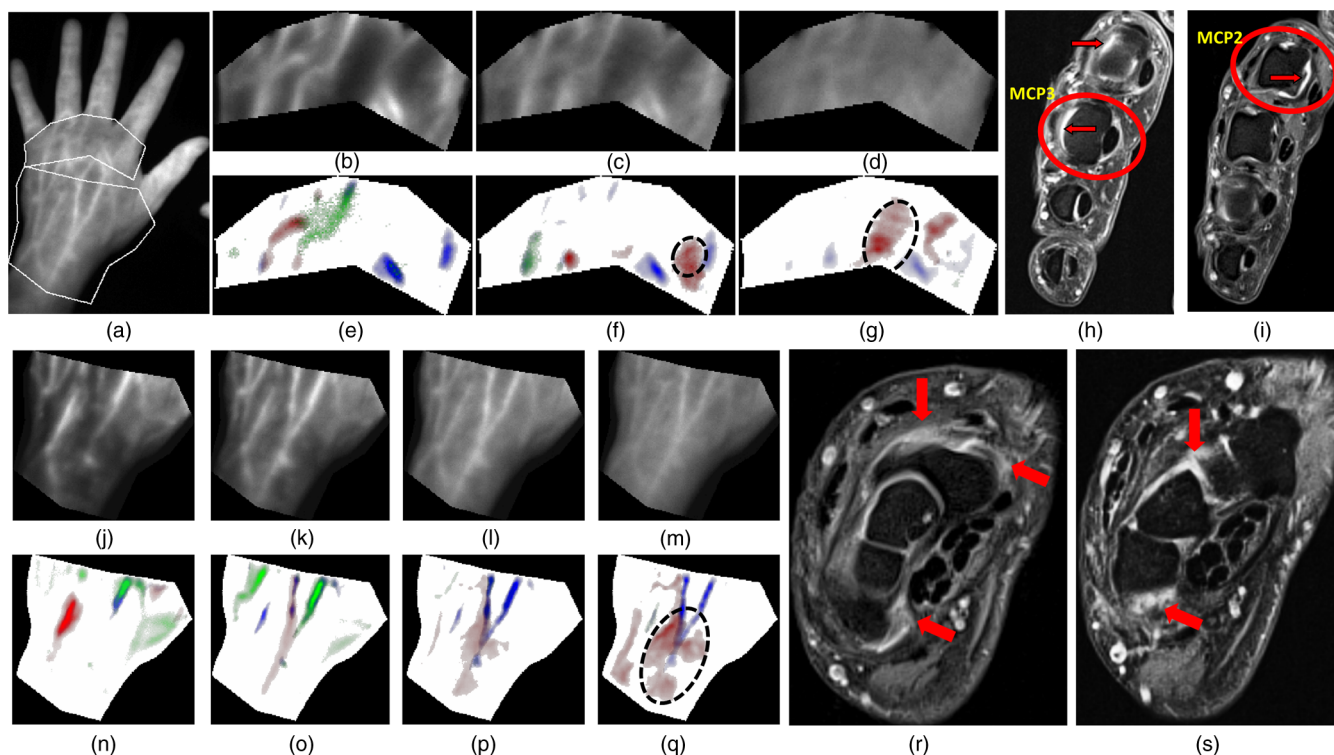


Fig. 7 Case study of a 49-year-old female patient with moderate synovitis in the left carpal and second MCP joints and mild synovitis in the third left MCP joint. (a) Sample fluorescence image at 100 s with MCP and carpal ROIs delineated by white lines. (b) to (d) Raw fluorescence images corresponding to time points 37, 52, and 99 s, respectively. (e) to (g) Corresponding processed colored images at the same three time points in the left MCP region. (h) to (i) transverse contrast-enhanced T1-weighted MR images of the MCP joints with the red arrows depicting the inflamed synovial lining in second and third MCP joints. The signal in the red channel specified by the dashed ellipses in (f) and (g) can be attributed to synovitis. Images (j) to (m) and (n) to (q) correspond to, respectively, raw and processed images of the carpus at time points 37, 48, 72, and 99 s. (r) and (s) show two transverse MR images of the carpus. The red channel signal in (q) delineated by the dashed ellipse can be associated with the moderate carpus synovitis.

components mapped to red, green, and blue channels. Moreover, Fig. 8(h) presents the T_1 -weighted MR findings for this patient as a coronal image of the carpus. No significant contrast due to a higher uptake of MR contrast agent can be observed in Fig. 8(h), and a synovitis score of 0 was subsequently assigned by the radiologist group (see Sec. 2.1 for explanation). The signal components appearing in the three color channels, corresponding to the three PCA components, of Figs. 8(b) to 8(d) are uncharacteristic of carpus synovitis and are attributable to veins or artifacts. In

this case, neither the raw fluorescence sequence nor the processed color images show any signal components typical of carpus synovitis. As observed in Table 1, the metric values for both processed and raw sequences are 0 for this case, that is, no localized component in the joint ROI was detected.

The data processing and simulations presented here were performed in 32 bit MATLAB on a Windows-based PC with a 2.3 GHz Intel CPU and 3.25 GB of RAM. The mesh generation, FEM modeling, and forward problem solution lasted,

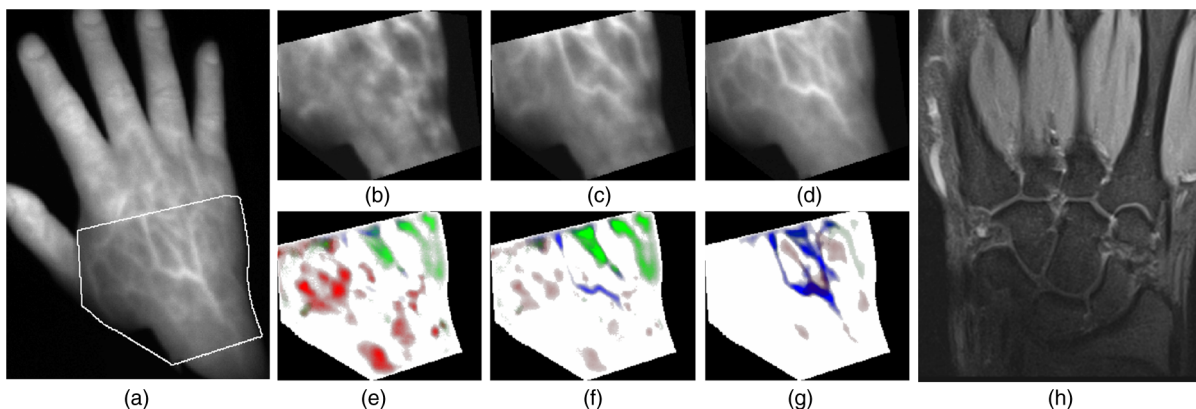


Fig. 8 Control case study of a 43-year-old male patient with healthy right carpal joint. (a) Sample fluorescence image at 100 s with carpal ROI delineated by white line. (b) to (d) Raw fluorescence images corresponding to time points 36, 42, and 61 s, respectively. (e) to (g) Corresponding processed colored images at the same four time points. (h) A coronal contrast-enhanced T1-weighted MR image of the carpus joints. The signal appearing in the red, blue, and green channels in (e) to (g) are due to veins or otherwise isolated spots, as in (e), and are uncharacteristic of carpus synovitis signal.

Table 2 Distribution of synovitis severity among the 450 hand joints of 10 patients and 5 healthy volunteers.

	Healthy	Mild inflammation (MR score of 1)	Moderate inflammation (MR score of 2)	Severe inflammation (MR score of 3)
Carpal joints	12	11	5	2
Metacarpophalangeal joints	59	73	17	1
Interphalangeal joints	235	28	6	1

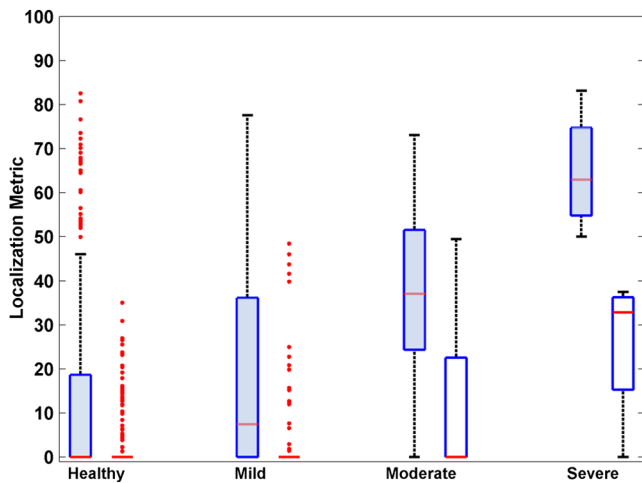


Fig. 9 Box plot of localization metric values assigned to raw and processed sequences for individual 450 joints of 10 patients and 5 healthy volunteers. The joints are grouped according to the severity of synovitis, where the left, blue boxes in each of the four groups correspond to processed sequences and the right boxes to raw sequences. Outliers are denoted by red points, the red line segment indicates the median, and box lower and upper edges are 25th and 75th percentile. In groups “healthy,” “mild,” “moderate,” and “severe,” there were 306, 112, 28, and 4 joints, respectively.

respectively, 60, 127, and 460 s. The processing of a given dataset consisting of 360 images took 110 s for all of 30 hand joints.

3.4 Spatiotemporal Analysis Applied to 450 Joints

The PCA-based processing method proposed in Sec. 2.2 was applied to fluorescence image sequences obtained from a group of 10 patients (7 females and 3 males, aged 51 ± 15) and 5 healthy volunteers (4 females and 1 male, aged 24 ± 2). The patients and volunteers were selected, examined, and imaged with contrast-enhanced MRI, and MR-based synovitis scores of 0 to 3 (healthy to severe) were assigned to each of the 450 joints, as explained in Sec. 2.1. The distribution of synovitis severity among different joint groups (carpal, MCP, and interphalangeal) are shown in Table 2. For each of the 450 joints, the localization metric was calculated for both the raw sequence and the processed sequences, as defined in Sec. 2.4. As a reminder, the metric has values in the range of 0 to 100, where a higher metric value indicates presence of a signal component in the corresponding sequence localized around the respective joint. Figure 9 presents a box-and-whisker plot of metric values for all joints grouped according to synovitis severity for both raw and processed sequences.

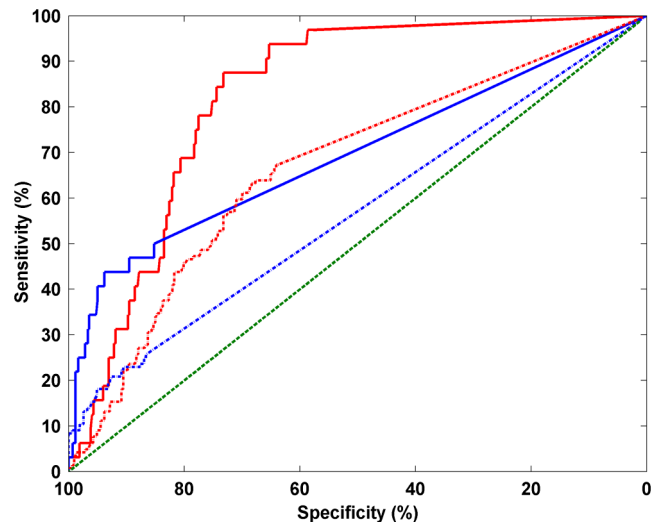


Fig. 10 Receiver operating characteristic (ROC) curves for localization metric values assigned to raw (blue curves) and processed (red curves) sequences for 450 joints of 10 patients and 5 healthy volunteers. The solid and dotted curves show classification performance for differentiating, respectively, between healthy and mild, moderate, or severe synovitis, denoted as classification I, and between healthy or mild synovitis and moderate and severe synovitis, denoted as classification II. The green dotted line represents random classification line of (sensitivity = 1 – specificity).

As the localization metric ranges between 0 and 100, a threshold can be applied to the localization metric to make a decision about synovitis severity of a given joint. For instance, given a threshold r , the joints with localization metric values larger than r can be classified as arthritic (consisting of all three levels of mild, moderate, and severe synovitis) and joints with metric values smaller than r can be classified as healthy. For a classifier defined as such and for a threshold value r , sensitivity and specificity can then be determined based on MR synovitis scores as the gold standard. Performing this analysis for all possible threshold values results in the receiver operating characteristic (ROC) curve, depicting sensitivity versus sensitivity = 1 – specificity.⁶² The corresponding ROC curves are presented in Fig. 10 for both raw (blue solid and dotted curves) as well as processed (red solid and dotted curves). The solid ROC curves denote sensitivity versus specificity when the threshold is applied to the metric to make a decision between “healthy” and “mild, moderate, or severe” synovitis, denoted here as classification I. The dotted ROC curves present sensitivity versus specificity when the decision is made between “healthy or mild synovitis” and “moderate or severe synovitis,” denoted here as classification II.

4 Discussion

Fluorescence images from RA patients and a healthy volunteer were analyzed for their intensity and their spatiotemporal characteristics also against MR images. It was found that PCA applied in time-series fluorescence images of the hand captured following intravenous ICG administration can decouple fluorescence signals associated with inflammation from the background and vein interference signals. Case studies were presented for eight carpal, MCP, and interphalangeal joints from four patients with varying degrees of synovitis (healthy to severe) presented in Secs. 3.2 and 3.3. Two patients had severe synovitis (MR-assigned synovitis score of 3) and one had mild to moderate synovitis (respective MR scores of 1 and 2) in carpal and MCP joints. One of the patients had moderate and mild synovitis in the second and fourth PIP joints of the left hand. One patient with healthy carpal joint, as verified by MRI, was shown to visually establish a control case study. The processing result along with the corresponding transverse or coronal images of contrast-enhanced T_1 -weighted MR images are presented in Figs. 5 to 8.

These findings were corroborated with numerical simulations based on a numerical phantom built using a segmented MR scan and were used to better understand the clinical findings. As expected, the contrast between the target and background fluorescence quickly falls with increasing depth and uptake ratio, as shown in Fig. 4(a). This reduces the detection sensitivity as was also observed by the localization metric surface in Fig. 4(b), which suggests lack of a localized signal component distinguishable as desirable fluorescence in the raw fluorescence measurements. It was found that a localized signal component appears in the joint region in at least one of the PCA components for lower depth and uptake ratios than in the original images, as shown in the dotted surface in Fig. 4(b), in a wider area in depth-uptake plane.

The impact of physical factors on the fluorescence signal was studied in Sec. 3.1. Observations of MR images of different patients revealed a synovial lining depth of 2 to 5 mm, 3 to 8 mm, and 7 to 16 mm for interphalangeal, MCP, and carpal joints, respectively. It can be seen from Fig. 8(a) that, even for relatively large uptake ratios, it is difficult to detect the desirable signal at locations deeper than ~ 5 mm due to the low relative contrast. These observations suggest low detectability of the targeted fluorescence signal in the raw fluorescence images for joints located deeper than 5 mm under skin, which can apply to some MCP and carpal joints. However, this conclusion does not necessarily mean that the fluorescence emanating from the inflammation of such joints cannot be distinguished in the raw images. The reason is that the numerical phantom presented in Sec. 2.3 does not render a full description of the *in vivo* situation. Factors such as heterogeneous and time-variant background fluorescence or nonuniform optical properties in tissue can degrade or improve the signal quality in comparison to predictions by the numerical model.

As noted, a low value of localization metric suggests presence of a signal component localized to the joint region and hence potentially attributable to the inflammation signal. While a higher metric value generally suggests improved performance in terms of signal visibility, the metric value cannot be interpreted as an indicator of the statistical sensitivity or specificity values. This observation means that the manifestation of a localized signal component in the joint regions, attributable to the synovitis signal, has been more frequent in the processed

sequences. However, the proposed method has a higher localization metric value for the healthy interphalangeal joints. This can be attributed to the dense dorsal vein network in the fingers, a fact that contributes to false positives and lowers sensitivity for the interphalangeal joints.

Corresponding analysis of the clinical data demonstrated that the contrast between synovial tissue and background tissue generally scaled with the severity of the disease; however, it diminished with time due to background nonspecific fluorescence signals. Subcutaneous dorsal veins demonstrated particularly high nonspecific signals; however, the entire tissue nonspecifically uptakes ICG and offers strong background signals. This reduction of contrast may lead to false positives or negatives, thus adversely affecting sensitivity. Similarly, fluorescence obtained from ICG circulating in the relatively dense subcutaneous venous network in interphalangeal joints further complicates the reading of raw images and may lead to reduced sensitivity and specificity.

Conversely, the PCA analysis revealed components linked to time-dependencies of the ICG circulation. Three components were identified to reveal clinically relevant time relationships. In particular, the first component demonstrated congruence with the appearance of increased fluorescence signals in joints. In other words, the first PCA component (i.e., the blue channel in the processed images) demonstrates consistent fluorescence signal increase in given joints. This was the case for fluorescence signals emanating from joints with moderate to severe synovitis demonstrated in Figs. 5 and 6. Signals from veins are also mapped to the first component for the same reason in Fig. 7. The second and third PCA components mapped, respectively, to the red and green channels in the processed images generally represent signal of transient nature. This temporally variable signal can arise from several sources. The fluorescence emanating from deep-seated lesions such as synovial lining, due to transitory accumulation of ICG, or the fluorescence carried quickly through veins can contribute to the second and third components. The transient, yet strong, signal emanating from dense vascular of fingertips also often contributes to red and green components, as seen in Figs. 5(n) to 5(q). Since the third component, represented by the green channel, corresponds to the lowest singular value and, hence, signal with lowest temporal correlation, it is generally expected to represent highly transient signals. The transient nature and, therefore, the level of information in the three PCA components are more pronounced at early time points, e.g., 20 to 100 s, after the injection. At later time points, such as after 120 s postinjection, the signal is mainly composed of the first PCA component and there is very little contribution from the second and third components, as the ICG has reached a relatively stable distribution in the hands and the signal experiences merely an exponential decay.

As explained, the temporal characteristics of the fluorescence signal in a given location in tissue impact the association of the fluorescence to a given PCA component. These temporal characteristics are mainly determined by the distribution of the ICG by the blood, as explained in Sec. 3.1, and other physiological factors such as tissue capillary permeability. However, it is not possible to attribute the fluorescence due to ICG presence in a certain tissue to a given PCA component.

The performance of the proposed approach is also limited by the physical factors of depth and uptake ratio. As with the raw fluorescence images, the interpretation of the processing results

is user-dependent. Characterization of certain signal components localized around the joint areas should be performed carefully so as not to lower diagnostic specificity. Furthermore, the presence of a strong transient or persistent signal component in a given joint might deteriorate the decoupling of the targeted fluorescence signals emanating from other joints. An example can be seen in the case study demonstrated in Fig. 7. The patient was diagnosed based on the MR images with moderate synovitis in the fourth and fifth left MCP joints. However, neither the raw data nor the processed sequence can indicate synovitis in these joints. This might be due to poor accumulation of ICG in the joint linings or interference from background tissue.

In Sec. 3.4, we presented imaging results for 450 joints of 5 healthy volunteers and 10 patients. The box plot demonstration of the localization metrics calculated for raw and processed sequences was presented in Fig. 9. As seen, the metric values calculated for the processed sequences generally correlate with severity of synovitis and are much higher than the corresponding values calculated using raw data for arthritis joints. The metric values for processed data from healthy joints are also lower for healthy joints than arthritic joints.

A more rigorous performance analysis was achieved using the ROC curves presented in Fig. 10. It can be seen that when differentiating between “healthy” and “mild, moderate, or severe” synovitis, denoted as classification I and corresponding to solid ROC curves in Fig. 10, classification using raw data is relatively close to random line (specificity = 1 – sensitivity). This is due to the fact that the target inflammation signal is almost always corrupted by interference from veins and other tissues, hence complicating observation of a localized signal component in the joint regions. The situation is better when differentiating between “healthy or mild synovitis” and “moderate or severe synovitis,” denoted as classification II, using raw data (corresponding to the dotted blue curves in Fig. 10). In fact for classification II, a specificity of 90% and a sensitivity of 44% can be achieved using the raw data. This is in accordance with the results of the clinical study presented in Ref. 41, which reports relatively low sensitivity (~39%) for a relatively high specificity (~85%) when differentiating between healthy and inflamed joints (classification I). It should be noted for specificity values >90%, the sensitivity values when using the raw data are slightly larger than when using the processed data, in both classifications I and II, though in all cases sensitivity is <45%. This is due to the fact that for healthy joints, more localized components have been detected in processed sequences than in raw data, as also seen in Fig. 9.

The area under the curve (AUC) values are found for the ROC curves presented in Fig. 10. For a given classifier ranking positive samples higher than negative ones, the AUC is equal to the probability of ranking a random positive sample higher than a random negative sample and is, hence, a measure of a classifier’s quality.⁶³ For classification I, AUC values of 0.57 and 0.67 were found when using, respectively, raw (dotted blue ROC curve) and processed (dotted red ROC curve) sequences. For classification II, AUC values of 0.69 and 0.83 were calculated when using, respectively, raw data (solid blue ROC curve) and processed data (solid red ROC curve). For the current dataset and specificity >60%, the sensitivity achievable for any threshold when using the raw data is limited to 25 and 50% for classifications I and II, respectively. However, when using the processed data, the sensitivity is limited to 65 and 94% for classifications I and II, respectively. These observations

suggest using the proposed PCA-based method results in superior clinical performance than relying on raw data for diagnosis.

It is important to note that the fluorescence image sequences are in practice analyzed and interpreted for diagnosis by specially trained human readers.^{26,41} The specificity and sensitivity values inferred from ROC curves of Fig. 10 serve to compare diagnostic value between raw and processed data. While the results demonstrate performance improvement when using the proposed method, the sensitivity and specificity of diagnosis performed by an expert human reader is expected to be higher than the values inferable from the ROC curves presented here. Furthermore, a cross-examination of both raw and processed sequences is likely to improve performance over using either sequence alone. A more complete clinical assessment of the proposed method requires examination of processed sequences by trained human readers for a clinically significant group of patients and is a subject of ongoing research.

In conclusion, the proposed method has the capability of differentiating between signal components that have different temporal behavior. This capability potentially enables separation of fluorescence emanating from tissue parts with different temporal and spatial profiles of ICG uptake. The interference from fluorescence in veins and the general tissue can be particularly mitigated, rendering the time-series analysis potentially as highly relevant to improve detection of inflamed joints compared to observing intensity images. The resulting color image sequences, when examined along with the original raw dataset, can help better localize the signal components due to the synovitis, hence improving diagnostic performance as shown by analysis of results of processing imaging data for 450 joints. The results of this work can also be employed to design next-generation optical systems and methods for imaging and detection of joint inflammation using exogenous fluorescence. Understanding the impact of physical and physiological factors on the detectability of the desirable fluorescence signal and the proposed numerical model can be employed to optimize the hand and finger posture during imaging. Moreover, the FEM-based time-series simulation framework can be employed to analyze the performance of other postprocessing approaches.

References

1. S. E. Gabriel, “The epidemiology of rheumatoid arthritis,” *Rheum. Dis. Clin. North Am.* **27**(2), 269–281 (2001).
2. M. A. Quinn and P. Emery, “Window of opportunity in early rheumatoid arthritis: possibility of altering the disease process with early intervention,” *Clin. Exp. Rheumatol.* **21**(Suppl 31), S154–S157 (2003).
3. M. Ostergaard, B. Ejlertsen, and M. Szkudlarek, “Imaging in early rheumatoid arthritis: roles of magnetic resonance imaging, ultrasonography, conventional radiography and computed tomography,” *Best Pract. Res. Clin. Rheumatol.* **19**(1), 91–116 (2005).
4. M. Backhaus et al., “Arthritis of the finger joints: a comprehensive approach comparing conventional radiography, scintigraphy, ultrasound, and contrast-enhanced magnetic resonance imaging,” *Arthritis Rheum.* **42**(6), 1232–1245 (1999).
5. P. Emery et al., “Finger tendon disease in untreated early rheumatoid arthritis: a comparison of ultrasound and magnetic resonance imaging,” *Arthritis Rheum.* **57**(7), 1158–1164 (2007).
6. W. T. Chen et al., “Arthritis imaging using a near-infrared fluorescence folate-targeted probe,” *Arthritis Res. Ther.* **7**(2), R310–R317 (2005).
7. A. D. Klose et al., “Two- and three-dimensional optical tomography of finger joints for diagnostics of rheumatoid arthritis,” *Proc. SPIE* **3566**, 151–160 (1999).

8. A. K. Scheel et al., "Assessment of proximal finger joint inflammation in patients with rheumatoid arthritis, using a novel laser-based imaging technique," *Arthritis Rheum.* **46**(5), 1177–1184 (2002).
9. T. Fischer et al., "Assessment of unspecific near-infrared dyes in laser-induced fluorescence imaging of experimental arthritis," *Acad. Radiol.* **13**(1), 4–13 (2006).
10. A. Hansch et al., "In vivo imaging of experimental arthritis with near-infrared fluorescence," *Arthritis Rheum.* **50**(3), 961–967 (2004).
11. A. H. Hielscher et al., "Sagittal laser optical tomography for imaging of rheumatoid finger joints," *Phys. Med. Biol.* **49**(7), 1147–1163 (2004).
12. T. Dziekan et al., "Detection of rheumatoid arthritis by evaluation of normalized variances of fluorescence time correlation functions," *J. Biomed. Opt.* **16**(7), 076015 (2011).
13. Y. Xu et al., "Imaging of in vitro and in vivo bones and joints with continuous-wave diffuse optical tomography," *Opt. Express* **8**(7), 447–451 (2001).
14. T. Fischer et al., "Detection of rheumatoid arthritis using non-specific contrast enhanced fluorescence imaging," *Acad. Radiol.* **17**(3), 375–381 (2010).
15. A. H. Hielscher et al., "Frequency-domain optical tomographic imaging of arthritic finger joints," *IEEE Trans. Med. Imaging* **30**(10), 1725–1736 (2011).
16. J. M. Lasker et al., "Dynamic optical imaging of vascular and metabolic reactivity in rheumatoid joints," *J. Biomed. Opt.* **12**(5), 052001 (2007).
17. Z. Yuan et al., "Image-guided optical spectroscopy in diagnosis of osteoarthritis: a clinical study," *Biomed. Opt. Express* **1**(1), 74–86 (2010).
18. Y. Sun, E. S. Sobel, and H. Jiang, "First assessment of three-dimensional quantitative photoacoustic tomography for in vivo detection of osteoarthritis in the finger joints," *Med. Phys.* **38**(7), 4009–4017 (2011).
19. J. R. Rajian, G. Girish, and X. Wang, "Photoacoustic tomography to identify inflammatory arthritis," *J. Biomed. Opt.* **17**(9), 096013 (2012).
20. E. Y. Ng and T. J. How, "Laser-Doppler imaging of osteoarthritis in proximal interphalangeal joints," *Microvasc. Res.* **65**(1), 65–68 (2003).
21. W. R. Ferrell et al., "Metacarpophalangeal joints in rheumatoid arthritis: laser Doppler imaging—initial experience," *Radiology* **220**(1), 257–262 (2001).
22. D. Chamberland, Y. Jiang, and X. Wang, "Optical imaging: new tools for arthritis," *Integr. Biol. (Camb)* **2**(10), 496–509 (2010).
23. L. L. Gompels et al., "In vivo optical imaging in arthritis—an enlightening future?," *Rheumatology (Oxford)* **49**(8), 1436–1446 (2010).
24. C. Bremer, S. Werner, and H. E. Langer, "Assessing activity of rheumatic arthritis with fluorescence optical imaging," *Eur. Musculoskeletal Rev.* **4**(2), 96–100 (2009).
25. R. Meier et al., "Indocyanine green—enhanced imaging of antigen-induced arthritis with an integrated optical imaging/radiography system," *Arthritis Rheum.* **62**(8), 2322–2327 (2010).
26. S. G. Werner et al., "Inflammation assessment in patients with arthritis using a novel in vivo fluorescence optical imaging technology," *Ann. Rheum. Dis.* **71**(4), 504–510 (2012).
27. J. S. Slakter et al., "Indocyanine green angiography of multifocal chorioiditis," *Ophthalmology* **104**(11), 1813–1819 (1997).
28. E. H. Kim et al., "Application of intraoperative indocyanine green video angiography to brain tumor surgery," *Acta Neurochir (Wien)* **153**(7), 1487–1495 (2011).
29. J. Caesar et al., "The use of indocyanine green in the measurement of hepatic blood flow and as a test of hepatic function," *Clin. Sci.* **21**, 43–57 (1961).
30. B. Ebert et al., "Cyanine dyes as contrast agents for near-infrared imaging in vivo: acute tolerance, pharmacokinetics, and fluorescence imaging," *J. Biomed. Opt.* **16**(6), 066003 (2011).
31. A. Raabe et al., "Near-infrared indocyanine green video angiography: a new method for intraoperative assessment of vascular flow," *Neurosurgery* **52**(1), 132–139 (2003).
32. V. Ntziachristos et al., "Concurrent MRI and diffuse optical tomography of breast after indocyanine green enhancement," *Proc. Natl. Acad. Sci.* **97**(6), 2767–2772 (2000).
33. G. C. Wishart et al., "A feasibility study (ICG-10) of indocyanine green (ICG) fluorescence mapping for sentinel lymph node detection in early breast cancer," *Ejso* **38**(8), 651–656 (2012).
34. C. Vinegoni et al., "Indocyanine green enables near-infrared fluorescence imaging of lipid-rich, inflamed atherosclerotic plaques," *Sci. Transl. Med.* **3**(84), 84ra45 (2011).
35. R. C. Benson and H. A. Kues, "Fluorescence properties of indocyanine green as related to angiography," *Phys. Med. Biol.* **23**(1), 159–163 (1978).
36. V. Ntziachristos, C. Bremer, and R. Weissleder, "Fluorescence imaging with near-infrared light: new technological advances that enable in vivo molecular imaging," *Eur. Radiol.* **13**(1), 195–208 (2003).
37. E. M. C. Hillman and A. Moore, "All-optical anatomical co-registration for molecular imaging of small animals using dynamic contrast," *Nat. Photonics* **1**(9), 526–530 (2007).
38. V. Ntziachristos et al., "Planar fluorescence imaging using normalized data," *J. Biomed. Opt.* **10**(6), 064007 (2005).
39. X. Intes et al., "In vivo continuous-wave optical breast imaging enhanced with indocyanine green," *Med. Phys.* **30**(6), 1039–1047 (2003).
40. V. Ntziachristos et al., "In vivo tomographic imaging of near-infrared fluorescent probes," *Mol. Imaging* **1**(2), 82–88 (2002).
41. R. Meier et al., "Detection of arthritis in the hands of patients with rheumatological disorders: diagnostic performance of optical imaging in comparison to MRI," *Arthritis Rheum.* **64**(8), 2489–2498 (2012).
42. I. T. Jolliffe, *Principal Component Analysis*, 2nd ed., Springer Series in Statistics, Springer, New York (2002).
43. A. S. Montcuquet et al., "Nonnegative matrix factorization: a blind spectra separation method for in vivo fluorescent optical imaging," *J. Biomed. Opt.* **15**(5), 056009 (2010).
44. J. Glatz et al., "Blind source unmixing in multi-spectral photoacoustic tomography," *Opt. Express* **19**(4), 3175–3184 (2011).
45. M. Ostergaard et al., "OMERACT rheumatoid arthritis magnetic resonance imaging studies. Core set of MRI acquisitions, joint pathology definitions, and the OMERACT RA-MRI scoring system," *J. Rheumatol.* **30**(6), 1385–1386 (2003).
46. V. Ntziachristos et al., "Concurrent MRI and diffuse optical tomography of breast after indocyanine green enhancement," *Proc. Natl. Acad. Sci. U. S. A.* **97**(6), 2767–2772 (2000).
47. P. Alliez et al., "3D mesh generation," in *CGAL User and Reference Manual*, CGAL Editorial Board (2011).
48. Q. Q. Fang and D. A. Boas, "Tetrahedral mesh generation from volumetric binary, and gray-scale images," in *2009 IEEE Int. Symp. on Biomedical Imaging: From Nano to Macro*, Vols. 1, and 2, pp. 1142–1145, IEEE (2009).
49. S. R. Arridge et al., "A finite element approach for modeling photon transport in tissue," *Med. Phys.* **20**, 299–309 (1993).
50. A. Ale et al., "FMT-XCT: in vivo animal studies with hybrid fluorescence molecular tomography-X-ray computed tomography," *Nat. Methods* **9**(6), 615–620 (2012).
51. Q. Zhang et al., "X-ray guided three-dimensional diffuse optical tomography: in vivo study of osteoarthritis in the finger joints," *Proc. SPIE* **6431**, 643112 (2007).
52. Y. Xu et al., "Three-dimensional diffuse optical tomography of bones and joints," *J. Biomed. Opt.* **7**(1), 88–92 (2002).
53. Z. Yuan et al., "Comparison of diffusion approximation and higher order diffusion equations for optical tomography of osteoarthritis," *J. Biomed. Opt.* **14**(5), 054013 (2009).
54. M. Levandowsky and D. Winter, "Distances between sets," *Nature* **234**(5), 34–35 (1971).
55. D. P. Huttenlocher, G. A. Klanderman, and W. J. Rucklidge, "Comparing images using the Hausdorff distance," *IEEE Trans. Pattern Anal. Mach. Intell.* **15**(9), 850–863 (1993).
56. R. Cárdenes, R. D. Luis-García, and M. Bach-Cuadra, "A multidimensional segmentation evaluation for medical image data," *Comput. Meth. Programs Biomed.* **96**(2), 108–124 (2009).
57. K. H. Zou et al., "Statistical validation of image segmentation quality based on a spatial overlap index—scientific reports," *Acad. Radiol.* **11**(2), 178–189 (2004).
58. W. R. Crum, O. Camara, and D. L. G. Hill, "Generalized overlap measures for evaluation and validation in medical image analysis," *IEEE Trans. Med. Imaging* **25**(11), 1451–1461 (2006).
59. K. Popuri et al., "3D variational brain tumor segmentation using Dirichlet priors on a clustered feature set," *Int. J. Comput. Assist. Radiol. Surg.* **7**(4), 493–506 (2012).

60. M. Basseville, "Distance measures for signal-processing and pattern-recognition," *Signal Process.* **18**(4), 349–369 (1989).
61. B. Hemery et al., "Comparative study of localization metrics for the evaluation of image interpretation systems," *J. Electron. Imaging* **19**(2), 023017 (2010).
62. K. H. Zou, A. J. O'Malley, and L. Mauri, "Receiver-operating characteristic analysis for evaluating diagnostic tests and predictive models," *Circulation* **115**(5), 654–657 (2007).
63. T. Fawcett, "An introduction to ROC analysis," *Pattern Recognit. Lett.* **27**(8), 861–874 (2006).